An initiative, simple vacancy remedy method and the effect on photochemical properties

Liquan Yang [a,b,e], Qi Xu [a,b,e], Fei Teng [a,b,c,d,e,*], Dongfang Yu [a,b,e], Yang Yang [a,b,e], Wenhao Gu [a,b,e], Yiran Teng [a,e], Jingjing Xu [a,e], Yan Guo [a,e]

[a] *Jiangsu Engineering and Technology Research Center of Environmental Cleaning Materials (ECM), Nanjing University of Information Science & Technology, 219 Ningliu Road, Nanjing 210044, China*
[b] *Jiangsu Collaborative Innovation Center of Atmospheric Environment and Equipment Technology (AEET), Nanjing University of Information Science & Technology, 219 Ningliu Road, Nanjing 210044, China*
[c] *Jiangsu Key Laboratory of Atmospheric Environment Monitoring and Pollution Control (AEMPC), Nanjing University of Information Science & Technology, 219 Ningliu Road, Nanjing 210044, China*
[d] *Jiangsu Joint Laboratory of Atmospheric Pollution Control (APC), Nanjing University of Information Science & Technology, 219 Ningliu Road, Nanjing 210044, China*
[e] *School of Environmental Science and Engineering, Nanjing University of Information Science & Technology, 219 Ningliu Road, Nanjing 210044, China*

ARTICLE INFO

ABSTRACT

Recently, an increasing attention is paid to crystal defects due to the significant influence on the catalytic properties of material. Herein, the WO_3 and fluorinated WO_3 (F-WO_3) samples have been prepared by an *in situ* hydrothermal method. On one hand, we have found that under visible light irradiation ($\lambda \geq 420$ nm), the photocatalytic activities of F-WO_3 samples are obviously reduced, which has been mainly attributed to the generation of W vacancies by fluorination. This finding is obviously distinct from the previous reports, in which the photocatalytic activities of semiconductors can be effectively improved by fluorination. On the other hand, after being further processed by H_2O_2 again, the generated W vacancies by fluorination can be remedied easily; moreover, the $WO_3/WO_3 \cdot 0.333H_2O$ heterojunctions have formed with a novel flower shape (H_2O_2-F-WO_3). It is amazing that under visible light irradiation ($\lambda \geq 420$ nm), the activity of H_2O_2-F-WO_3 sample is 4.3 and 3.0 times higher than that of F-WO_3 and WO_3, respectively. The significantly improved activity is mainly attributed to the remedy of W vacancy and the formation of the $WO_3/WO_3 \cdot 0.333H_2O$ heterojunction. Compared with conventional defect remedy method (*e.g.*, calcination), this vacancy remedy method with H_2O_2 is facile, energy-saving, which could be extended to develop the other efficient photocatalysts.

© 2016 Elsevier B.V. All rights reserved.

1. Introduction

As an advanced oxidation technology, solar energy-driven photocatalysis has drawn considerable attention. Unfortunately, its practical application is still limited by the low utilization of solar energy and low quantum efficiency. In the past decades, various strategies have been tried to solve the problems, such as band gap engineering, crystal modification, interfacial heterojunction, and so on [1]. However, it is still a big challenge to develop efficient photocatalysts.

Recently, tungsten trioxide (WO_3) has attracted much attention due to its abundant reserves, nontoxicity and excellent optical property [2–6]. As an n-type semiconductor, WO_3 ($E_g = 2.5$–2.8 eV) exhibits approximately 12% absorption of solar energy [2]. Because of its low conduction band edge (0.3–0.5 *vs.* normal hydrogen electrode (NHE)), however, the conduction band electrons of WO_3 cannot react with O_2 ($E_0(O_2/O_2^{\bullet-}) = -0.33$ *vs.* NHE and $E_0(O_2/HO_2^{\bullet}) = -0.05$ *vs.* NHE) [7–9]. Consequently, its photocatalytic activity is significantly reduced by the fast recombination rate of electrons and holes. Hence, it is desirable to develop a new method to solve this disadvantage. To date, many studies have reported that the fluorination of semiconductor can efficiently enhance the photocatalytic activities [1,10–16], *e.g.*, TiO_2 [10–13],

Bi_2O_3 [14], $BiPO_4$ [15], $ZnWO_4$ [16], *etc*. Nevertheless, the fluorination of WO_3 has not been reported to date. Hence, it is still unknown for us whether fluorination can improve photocatalytic activity of WO_3 or not. It has been reported that the doping of fluorine can introduce special localized electronic and surface defect states [12,17]. For instance, the fluorine-doped TiO_2 shows a visible light activity due to the creation of surface oxygen vacancies [10,12]. In this work, W vacancies, instead of surface oxygen vacancies, are generated by the fluorination of WO_3. However, we have found that the W vacancies are disadvantageous to the photocatalytic reaction. Generally, crystal defects can be repaired by a calcination method [18]. Nevertheless, the calcination method often brings about the significant changes in particle size and morphology [19], leading to a poor physicochemistry properties. Besides, the fluorine within crystal lattices is easy to be removed during calcination [20]. Thus, it is desirable to develop a mild method for the vacancy remedy, so as to obtain an efficient photocatalyst.

In this work, we have developed a new, mild approach to remedy W vacancies, in which the $[O_2]^{2-}$ chelating ligand can be provided by H_2O_2 [21]. It is found that after being processed with H_2O_2, two interesting results are obtained as follows: (1) the W vacancies generated by the fluorination of WO_3 can be remedied by H_2O_2; (2) a heterojunction can form between monoclinic WO_3 and orthorhombic $WO_3 \cdot 0.333H_2O$ with a new flower shape. This facile post-synthesis defect remedy method may be extended to develop the other efficient photocatalysts.

2. Experimental

2.1. Sample preparation

All reagents were of analytical grade, purchased from Beijing Chemical Reagents Industrial Company of China, and were used without further purification.

2.1.1. Synthesis of WO_3 and F-WO_3

The WO_3 and fluorinated WO_3 (F-WO_3) samples were synthesized by a simple hydrothermal method. Typically, 1.3 g of ammonium tungstate, the measured amount of NH_4F and 5 mL 65 wt% nitric acid were added in 20 mL of deionized water in sequence. After being stirring for 30 min, the mixture was transferred into Teflon-lined stainless steel autoclaves and heated at 180 °C for 24 h; then the resulting precipitate was collected by centrifugation, washed with deionized water for several times, and finally dried at 60 °C. To investigate the effect of the NH_4F amount added, the atomic ratio (R_F) of F to W was varied from 0 to 0.1, 0.5, 1.0 and 2.0. Herein, the as-prepared sample at $R_F = 0$ is designated as WO_3, while the as-prepared samples at $R_F = 0.1$–2.0 are designated as F-WO_3.

2.1.2. Post-synthesis processing with H_2O_2

Typically, the as-synthesized F-WO_3 ($R_F = 1.0$) or WO_3 ($R_F = 0$) above was added in the mixture solution containing both 10 mL of 30 wt% H_2O_2 and 5 mL of H_2O. Then, the mixture solution was transferred into Teflon-lined stainless steel autoclaves, and was processed at 180 °C for 24 h. After reaction, the resulting precipitate was collected by centrifugation, washed with deionized water, and dried at 60 °C. Herein, the as-processed WO_3 and F-WO_3 samples are designated as H_2O_2-WO_3 and H_2O_2-F-WO_3, respectively.

2.2. Characterization

The crystal structures of the samples were determined by X-ray powder polycrystalline diffractometer (Rigaku D/max-2550VB), using graphite monochromatized Cu K_α radiation ($\lambda = 0.154$ nm), operating at 40 kV and 50 mA. The XRD patterns were obtained in the range of 10–80° (2θ) at a scanning rate of 7° min^{-1}. The samples were characterized on a scanning electron microscope (SEM, Hitachi SU-1510) with an acceleration voltage of 15 keV. The samples were coated with 5-nm-thick gold layer before observations. The fine surface structures of the samples were determined by high-resolution transmission electron microscopy (HRTEM, JEOL JEM-2100F) equipped with an electron diffraction (ED) attachment with an acceleration voltage of 200 kV. X-ray photoelectron spectroscopy (XPS) measurements were done on a VG ESCALAB MKII XPS system with Mg K_α source and a charge neutralizer. All the binding energies were referenced to the C1 s peak at 284.8 eV of the surface adventitious carbon. Electron paramagnetic resonance (EPR) spectra were conducted on a Bruker ESP 500 spectrometer at room temperature. UV–vis diffused reflectance spectra of the samples were obtained using a UV–vis spectrophotometer (UV-2550, Shimadzu, Japan). $BaSO_4$ was used as a reflectance standard in a UV–vis diffuse reflectance experiment. Nitrogen sorption isotherms were performed at 77 K and $<10^{-4}$ bar on a Micromeritics ASAP2010 gas adsorption analyzer. Each sample was degassed at 90 °C for 5 h before measurements. Nitrogen adsorption–desorption isotherms were obtained at 77 K using the Autosorb-iQ physicoadsorption apparatus (Quantachrome). Surface area was calculated by the Brunauer-Emmett-Teller (BET) method.

An electrochemical system (CHI-660B, China) was employed to measure the electrochemical impedance spectroscopy (EIS) and photocurrent. EIS was performed from 0.1 Hz to 100 kHz at an open circuit potential of 0.3 V and alternating current (AC) voltage amplitude of 5 mV. The data were analyzed by Zsimwin software. Photocurrent measurement was carried out in a conventional three-electrode system, in which indium-tin oxide (ITO) glass was used as the current collector to fabricate photo electrode, and 0.1 M Na_2SO_4 was used as the electrolyte solution. The sample/ITO photo electrodes were prepared by a dip-coating method. The photo electrode was implemented as the photo anode in a photoelectrochemical cell (PEC).

2.3. Theoretical calculations

The simulations of band structures, total and partial densities of states (T- and P-DOS) were calculated by density functional theory (DFT) as implemented in the CASTEP. The calculations were carried out using the generalized gradient approximation (GGA) level, and Perdew-Burke-Ernzerh (PBE) formalism for combination of exchange and correlation function. The cut-off energy is chosen as 380 eV, and a density of $(3 \times 2 \times 5)$ Monkhorst-Pack K-point was adopted to sample the Brillouin zone.

2.4. Photocatalytic activity measurements

The photocatalytic activity of the sample was performed under visible light irradiation ($\lambda \geq 420$ nm). 0.1 g of photocatalyst was put into a 250-mL beaker containing 200 mL of 10 mol L^{-1} methyl blue (or rhodamine b) dye solution. A 500-W high pressure Xe lamp (Beijing ZhongjiaoJinyuan Science Co. Ltd. China) was used as light source. The breaker was placed in a sealed black box with the top opened, and the distance between the breaker and light source was 15 cm. Before the lamp was turned on, the suspension was continuously stirred for 30 min in the dark to ensure the establishment of an adsorption–desorption equilibrium between the catalyst and dye. During degradation, 3 mL of the solution was collected using a pipette at intervals of irradiation, and subsequently centrifuged to remove the catalyst. UV–vis spectra were recorded using a Spectrumlab 722sp spectrophotometer to determine the concentration of dye.
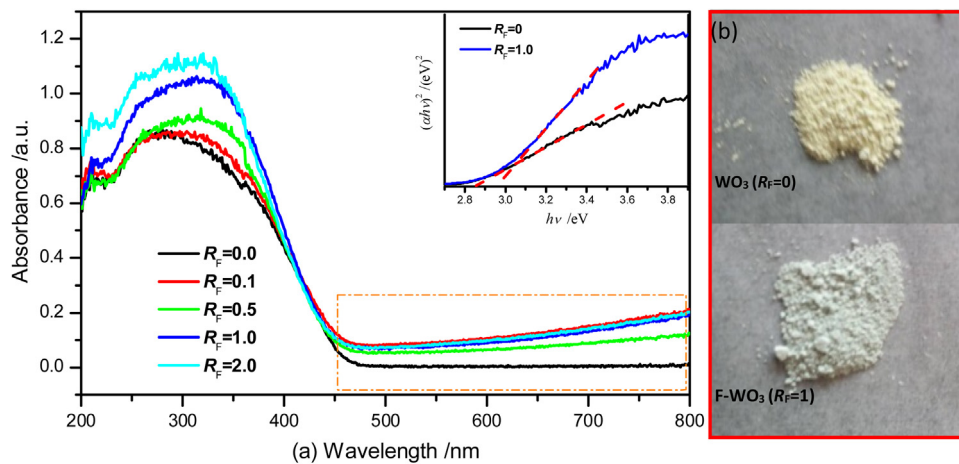
Fig. 1. (a) Ultraviolet–visible diffuse reflectance spectra (UV-DRS) of the samples prepared at different R_F: the inset of Tauc plots ($(\alpha h\nu)^2$ *vs.* energy) of WO_3 at $R_F = 0$ and F-WO_3 at $R_F = 1.0$; (b) Photographic colors of the samples at $R_F = 0$ and 1.0; R_F: Atomic ratio of F to W.

3. Results and discussion

3.1. Physico-chemistry and vacancy property of the samples

3.1.1. UV-DRS spectra

Fig. 1 shows the Ultraviolet–visible diffuse reflection spectra (UV-DRS) of the samples at different R_F. Compared with pure WO_3, all the F-WO_3 samples show obvious light absorptions above 450 nm (Fig. 1a), which may originates from the surface defect states of F-WO_3 [22,23]. Typically, the inset of Fig. 1a shows the Tauc plots ($(\alpha h\nu)^2$ *vs.* energy) of WO_3 at $R_F = 0$ and F-WO_3 at $R_F = 1.0$. Their band gaps are determined to be 2.86 and 2.97 eV for WO_3 and F-WO_3, respectively. Moreover, the presence of surface defects can also be confirmed by their different apparent colors. The WO_3 sample prepared at $R_F = 0$ is yellow, but the F-WO_3 sample at $R_F = 1$ is grayish green (Fig. 1b). The weak absorption above 420 nm has also been observed for the other fluorinated photocatalysts [10,15,16]. This result also confirms the presence of defects in the F-WO_3 sample. It is obvious that the fluorination has a significant influence on the light absorption of the sample.

3.1.2. XRD analysis

Fig. 2a shows X-ray diffraction (XRD) patterns of the samples at different R_F. All the samples are composed of phase-pure mon-oclinic WO_3 (JCPDS No. 83-0951). Moreover, Fig. 2b shows the zoom-in XRD patterns in the range of $2\theta = 22$–$25°$. Some distinguishing features can be observed at different R_F as follows. First, the (002) peak slightly shifts to a higher 2θ value with the increase of R_F. According to Bragg's law (1) as follows:

$$2d\sin\theta = n\lambda \tag{1}$$

where, n is the reflection order, λ is the wavelength of the incidence ray, d is the interplanar spacing and θ is the incidence angle. Generally, the increase and decrease of 2θ result from the shrinkage and expansion of cell or lattice, respectively. With increasing R_F, the slight right shift of (002) peak form $23.16°$ to $23.26°$ suggests that one O^{2-} may be substituted by only one F^- (designated as: one-one), because the radius (0.133 nm) of F^- is slightly smaller than that (0.140 nm) of O^{2-} [14]. To keep the charge balance, this one–one substitution would lead to the formation of W vacancies in the WO_3 host [14].

Second, the broadening of diffraction peaks in the 2θ range of 23.5–$24.75°$ can also be observed with increasing R_F, indicating a reduced crystallinity [24]. By using Gaussian fitting method, the broadening peaks can be well fitted to the (200) peak and a new peak. With increasing of R_F, the (200) peak becomes weaker, but the new peak becomes stronger and shifts to a lower 2θ value from $24.40°$ to $23.99°$. In order to further understand the newly-formed
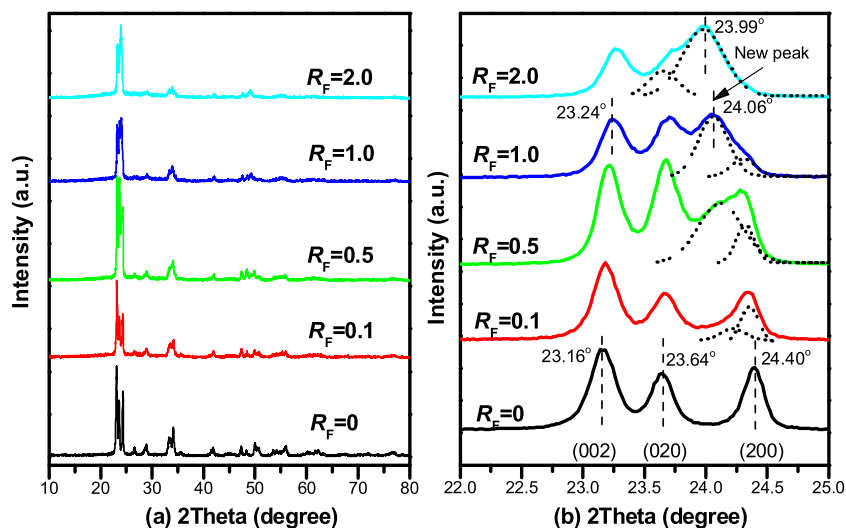
Fig. 2. XRD patterns of the as-prepared samples at deferent R_F: (a) $2\theta = 10$–$80°$; (b) $2\theta = 22$–$25°$.
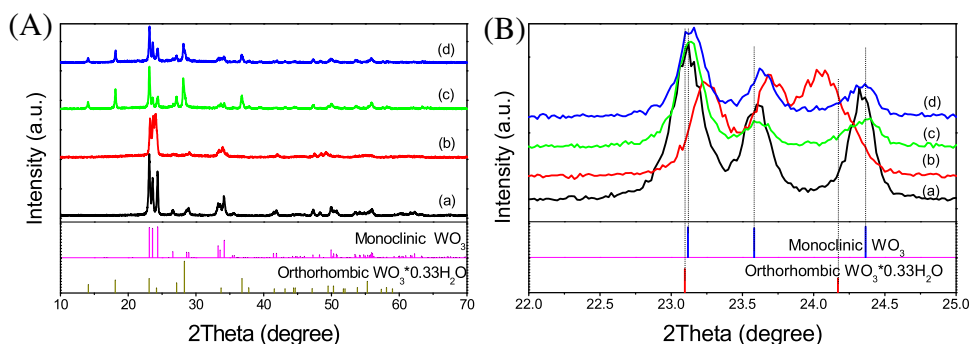
Fig. 3. XRD patterns of the samples in the scanning ranges of (A) 10–70° and (B) 22–25°: (a) WO_3 ($R_F = 0$, monoclinic WO_3); (b) F-WO_3 ($R_F = 1$, monoclinic WO_3); (c) H_2O_2-WO_3 ($R_F = 0$, $WO_3/WO_3 \cdot 0.333H_2O$); (d) H_2O_2-F-WO_3 ($R_F = 1$, $WO_3/WO_3 \cdot 0.333H_2O$).

peak, we have mainly choose the F-WO_3 sample at $R_F = 1$ as an example to analyze. Its (002) peak and newly-formed peak locate at 23.24° and 24.06°, respectively. The calculated lattice spacings of (002) peak and the new peak by Bragg's law (1) are 0.382 nm and 0.370 nm, respectively. Herein, we assume that the new peak is relative to the formation of W vacancies, which will be further confirmed by HRTEM in the next section.

3.1.3. SEM and HRTEM analyses

Typically, the WO_3 ($R_F = 0$) and F-WO_3 ($R_F = 1$) are further processed by H_2O_2. Fig. S1 (electronic Supporting information (ESI)) shows the scanning electron microscopy (SEM) images of the samples. It is observed that the WO_3 and F-WO_3 samples are composed of nanoparticles and nanosheets, respectively; but the H_2O_2-WO_3 and H_2O_2-F-WO_3 samples are both composed of the flowers. Further, Fig. 3 shows their XRD patterns. Before being processed with H_2O_2, the WO_3 ($R_F = 0$) and F-WO_3 ($R_F = 1$) are both composed of monoclinic WO_3 (JCPDS No. 83-0951). After processing, the H_2O_2-WO_3 and H_2O_2-F-WO_3 samples are both composed of orthorhombic $WO_3 \cdot 0.33H_2O$ (JCPDS No. 35-0270) and monoclinic WO_3 (JCPDS No. 83-0951) phases.

Moreover, the F-WO_3 ($R_F = 1$) and H_2O_2-F-WO_3 samples are characterized by high-resolution transmission microscopy (HRTEM) (Fig. 4). For the F-WO_3 sample (Fig. 4(a–d)), the lattice spacings of the top and bottom surfaces of nanosheets are determined to be 0.383 and 0.262 nm, corresponding to (002) and (202) planes, respectively. The lateral surface of nanosheet is shown in Fig. 4d. The lattice spacing of the lateral surface of nanosheet

is determined to be 0.374 nm, corresponding to (020) plane. The results above indicate that the top and bottom plane of nanosheet are enclosed by {010}. On the top surface of nanosheet (Fig. 4(a,b)), the lattices fringes of the nanosheet are indiscernible, indicating the formation of defects. In Fig. 4c, it is noteworthy that the part of lattices become loose, compared with the closely-packed lattices around. Along the [200] direction, the loose lattice spacings are determined to be 0.370 nm, which is exactly equal to the lattice spacings of the new peak calculated by using Bragg's law (1) above; however, the spacings of the close-packed lattice are 0.364 nm, corresponding to the (200) plane. The increase of lattice spacings can be understood as follows: WO_3 consists of WO_6 octahedral units by sharing corner, edge and face [2,24], as shown in Fig. S2 (ESI). This structure means that the crystal lattices of WO_3 are able to endure a considerable amount of oxygen vacancies present in crystal [24]. Thus, many non-stoichiometric $WO_{x < 3}$ have been reported [2,24], e.g., $WO_{2.9}$ [25], $WO_{2.83}$, $WO_{2.72}$, etc. Herein, we can easily understand that WO_6 octahedral units are still stable, when F^- and W vacancies are introduced. Herein, the lattice sapcing of {200} becomes slightly larger (0.364 vs. 0.370 nm), through the self-adjustment of F, O and W vacancy. Herein, we could assume that the new peaks in XRD patterns are relative to the W vacancy that increases with the increase of R_F.

Fig. 4(e–h) shows the HRTEM images of the H_2O_2-F-WO_3 sample. The H_2O_2-F-WO_3 sample also shows the flower morphology. The clear lattice fringes correspond to the (002) plane of $WO_3 \cdot 0.333H_2O$ and the (200) plane of WO_3, respectively. This clearly confirms the formation of $WO_3/WO_3 \cdot 0.333H_2O$ heterojunc-
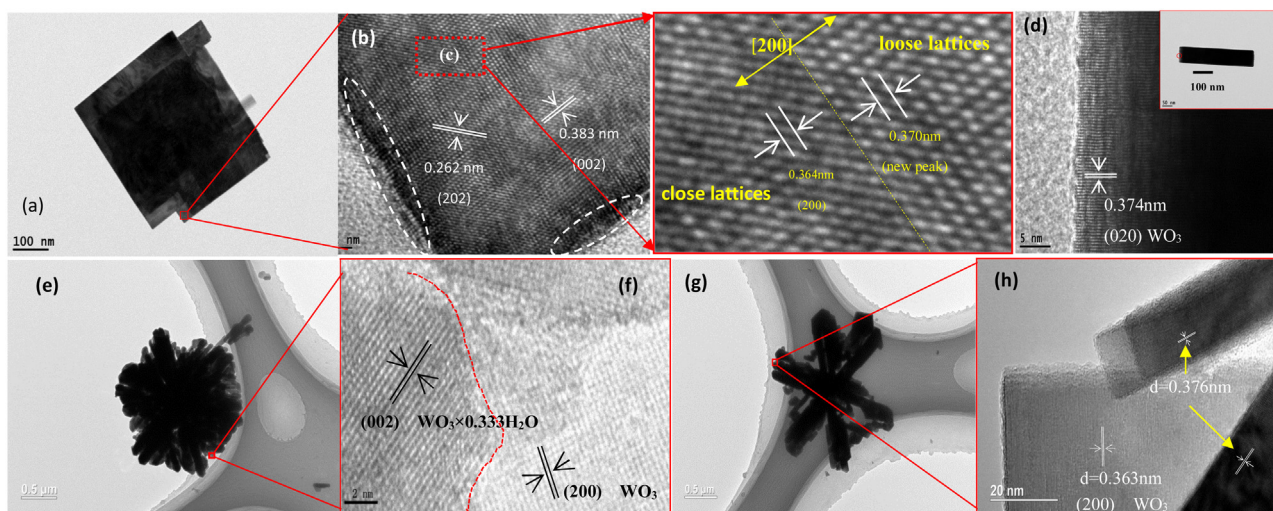
Fig. 4. HRTEM images of the samples: (a–d) F-WO_3 ($R_F = 1$); (e–h) H_2O_2-F-WO_3.
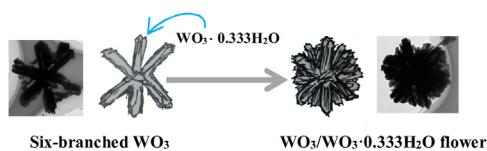
Fig. 5. Schematic transform diagram from six-branched WO_3 to $WO_3/WO_3 \cdot 0.333H_2O$ flower.

tions (Fig. 4(e,f)). In Fig. 4(g,h), it is noteworthy that the six branched H_2O_2-F-WO_3 flower are also observed. The lattice spacings of the main branch are determined to be 0.363 nm and 0.376 nm, corresponding to the (200) and (020) planes of WO_3, respectively. This indicates that the main branch of the H_2O_2-F-WO_3 flower is made of monoclinic WO_3 phase. Compared with Fig. 4(e,f), the sub-branches are composed of the $WO_3/WO_3 \cdot 0.333H_2O$ heterojunctions, which attach to the main branches to form the flower. The schematic transform diagram is shown in Fig. 5. Compared with the F-WO_3 nanosheets ($R_F = 1$), the lattice spacing (0.370 nm) of the new peak is not detected for the flower, suggesting that the W defects are remedied after being processed with H_2O_2.

Finally, Fig. S3 (ESI) shows the HRTEM images of the H_2O_2-WO_3 sample. At the edge of the H_2O_2-WO_3 sample, two sets of lattice fringe spacings correspond to the (222) plane of monoclinic WO_3 and the (202) plane of monoclinic $WO_3 \cdot 0.333H_2O$, also confirming the formation of a heterojunction.

3.1.4. XPS spectra and EPR

Typically, X-ray photoelectron spectrum (XPS) and electron paramagnetic resonance (EPR) are performed to further verify the defect structure of the as-synthesized samples (Fig. 6). First, Fig. S4 (ESI) shows the XPS survey spectrum of the samples. The XPS surface elements analysis is summarized in Table 1. The atomic ratio of O to W is 2.81 for the as-prepared WO_3 sample ($R_F = 0$), but 3.32 for F-WO_3 ($R_F = 1$). The decrease of W atom suggests the generation of W vacancies in F-WO_3 ($R_F = 1$). After the F-WO_3 ($R_F = 1$) sample is processed with H_2O_2, the atomic ratio of O to W is 2.99 for the H_2O_2-F-WO_3 sample, which is obviously closer to that of WO_3 but higher than F-WO_3, indicating that the processing with H_2O_2 has remedied the W vacancies. Since $[O_2]^{2-}$ has a strong chelating ability, WO_3 can dissolve in H_2O_2 solution. This post-synthesis processing reaction, in fact, involves the re-dissolution and re-crystallization processes, during which, superfluous O atoms may release to the solution. Consequently, W vacancies are successfully remedied.

Second, Fig. 6(a,b) show the O 1s and W 4f signals of the WO_3, F-WO_3 and H_2O_2-F-WO_3 samples. For the H_2O_2-F-WO_3 sample, the O1s peak at 532.6 eV can be ascribed to the O—H groups associated with the crystal water [24]. Compared with the WO_3 sample ($R_F = 0$), the O 1s, W4f5/2 and W4f7/2 binding energies of the F-WO_3 ($R_F = 1$) and H_2O_2-F-WO_3 samples increase about 0.3 eV. This is caused by the changed chemical environment around O and W due to the partial substitution of F^- for O^{2-}, which has been reported ever by the other researchers [14,20]. Moreover, the F-WO_3 ($R_F = 1$) and H_2O_2-F-WO_3 samples have the almost same binding energies of O1s and W4f, indicating that the substitution of F^- for O^{2-} still exists after being processed by H_2O_2. Further, Fig. 6c shows the

typical F 1s spectra of the WO_3 ($R_F = 0$) and F-WO_3 ($R_F = 1$) samples. It has been reported that the weak and broad F1s peaks at binding energies of around 684.9 eV and 687.6 eV are mostly originated from the physically adsorbed F on the crystal surface and the doped F in crystal, respectively [17,26–28]. However, the F 1s signal is too weak to be detected for our F-WO_3 sample. Herein, two main reasons can be considered as follows: First, it may be that the concentration of the doped F in WO_3 is too low to be detected by XPS; Second, the XPS analysis can only detect the atoms of surface layer with the depth about 2–5 nm. Moreover, our XRD patterns have confirmed that the F has doped in the lattices of F-WO_3 ($R_F = 1$).

Third, Fig. 6d presents the electron paramagnetic resonance spectrum (EPR) of the F-WO_3 ($R_F = 1$) sample. EPR is a well-established technique to probe the defects like O vacancies [29,30], where the EPR signal is derived from the trapped unpaired electrons. Because no signal is detected for the four samples, we could deduce that W vacancy may be not paramagnetic, namely, the W vacancy does not contain the unpaired electrons, which is different from the oxygen vacancy [29,30].

3.2. Photocatalytic activity

3.2.1. Adsorption and degradation of MB

First, we have investigated the adsorption properties of methylene blue (MB) over the as-prepared samples at different R_F and their degradation activities under visible light irradiation ($\lambda > 400$ nm), as shown in Fig. 7a. After irradiation for 80 min, the degradation percentage of MB is around 90% by the WO_3 ($R_F = 0$) sample, whereas the degradation percentages of all the F-WO_3 samples are lower than 60%, which may be ascribed to the formation of bulk W vacancies.

Meanwhile, it is well-known that adsorption ability is an important factor influencing the photocatalytic activity of photocatalyst. Thus, the adsorption percentages of MB over the samples are also illustrated in Fig. 7a. Adsorption is mainly relative to the surface properties of photocatalyst [31,32]. Compared with the WO_3 ($R_F = 0$) sample, all the F-WO_3 samples show slightly higher adsorption abilities, suggesting the formation of favorable surface under fluorination.

3.2.2. Degradation of RhB

Moreover, we have mainly investigated the photocatalytic performances of the WO_3 ($R_F = 0$), H_2O_2-WO_3, F-WO_3 ($R_F = 1$) and H_2O_2-F-WO_3 samples under visible light irradiation ($\lambda \geq 420$ nm) using rhodamine B (RhB) as the probing molecule, as shown in Fig. 7b. It is observed that the photocatalytic activities of the samples follow the order as follows: H_2O_2-F-$WO_3 > H_2O_2$-$WO_3 \gg WO_3 > $ F-WO_3. The photocatalytic activity of a photocatalyst is affected by many factors. First of all, BET area is an important factor to influence the activity. As shown in Table 1, all the samples have almost the similar BET areas (WO_3: 6.6 $m^2 g^{-1}$, F-WO_3: 7.0 $m^2 g^{-1}$; H_2O_2-WO_3: 7.2 $m^2 g^{-1}$; H_2O_2-F-WO_3: 7.1 $m^2 g^{-1}$), suggesting that the BET area may not be the crucial factor for the different activities.

First, the F-WO_3 ($R_F = 1$) sample shows a slightly lower photocatalytic activity than the WO_3 ($R_F = 0$) sample for the degradations

Table 1
XPS surface elements analysis and BET areas of the samples.

Samples	BET area[a] (m^2/g)	Phase compositions	O atom%	W atom%	O:W (atom ratio)
WO_3	6.6	monoclinic WO_3	37.17	13.22	2.81:1
F-WO_3	7.0	monoclinic WO_3	61.262	18.457	3.32:1
H_2O_2-WO_3	7.2	$WO_3/WO_3 \cdot 0.333H_2O$	/	/	/
H_2O_2-F-WO_3	7.1	$WO_3/WO_3 \cdot 0.333H_2O$	32.08	10.74	2.99:1

[a] Calculated by the Brunauer–Emmett–Teller (BET) method.
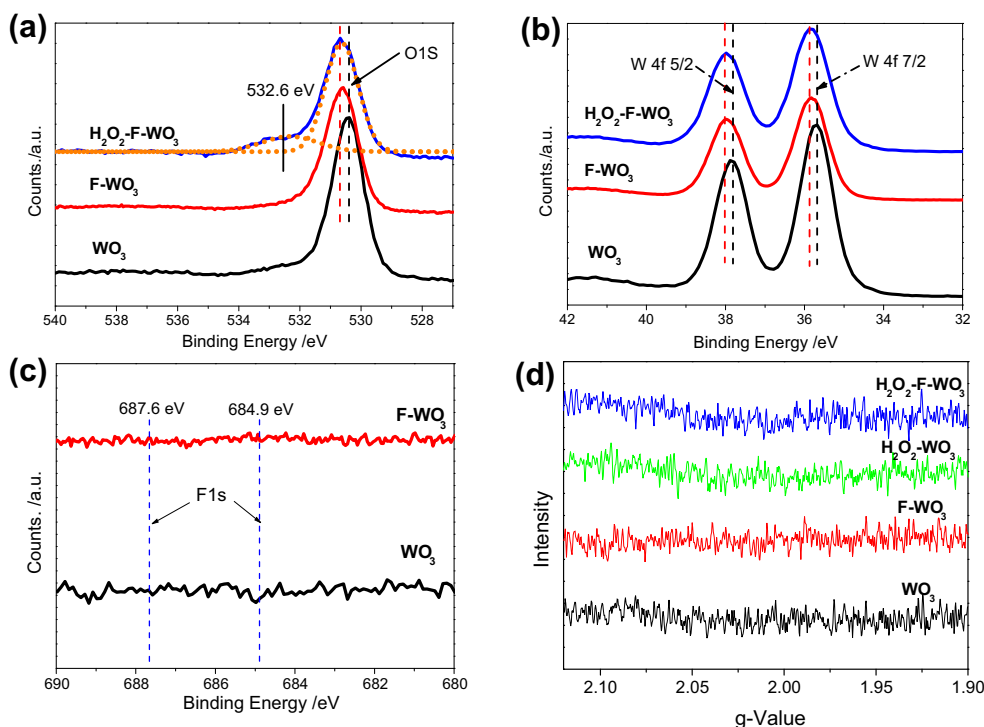
Fig. 6. (a–c) X-ray photoelectron spectra (XPS) of WO_3 ($R_F = 0$), F-WO_3 ($R_F = 1$) and H_2O_2-F-WO_3 ($R_F = 1$): (a) O 1s; (b) W 4f; (c) F 1s XPS spectra of WO_3 and F-WO_3; (d) Electron paramagnetic resonance (EPR) spectra of the samples.
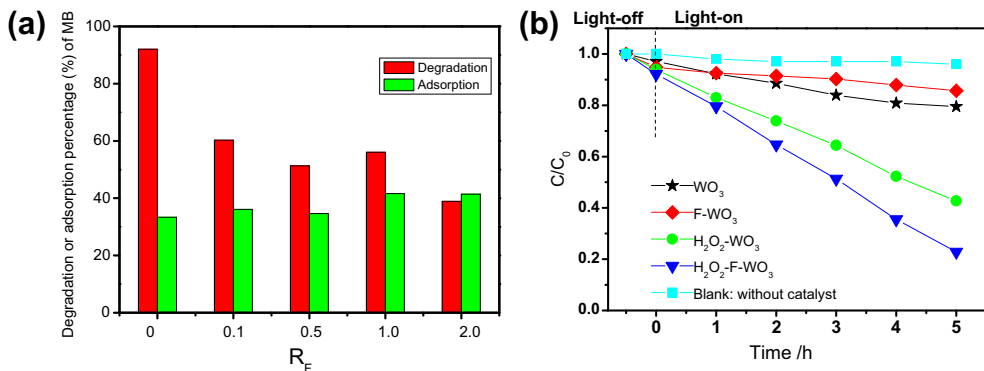

Fig. 7. Adsorption and photocatalytic degradation performances of the samples under visible light irradiation ($\lambda > 420$ nm): (a) MB; (b) RhB.

of RhB under visible-light irradiation. To understand this result, the photocurrent and electrochemical impedance spectroscopy analyses are further investigated, as shown in Fig. 8. The photocurrent is commonly used to investigate the separation and transfer processes of charges. Under visible light irradiation ($\lambda \geq 400$ nm) (Fig. 8a), an extremely lower photocurrent is generated over the F-WO_3 sample ($R_F = 1$), which is only about one twelfth of that of the WO_3 sample ($R_F = 0$). The result suggests that the F-WO_3 sample ($R_F = 1$) has much lower separation and transfer rates of electron [16]. It has been reported that bulk defects like O vacancies usually act as the recombination centers for the photo-generated electrons and holes, thus reducing photocatalytic activity. Herein, we hold that, similar to the bulk O vacancies, the bulk W vacancies may be the recombination centers of electrons and holes, thus reducing photocurrent and photocatalytic activity [18,33,34]. However, it should be noted that the real effect of W vacancies is intricate and not easy to characterized, which needs extensive research in

future. The photocurrent over the H_2O_2-F-WO_3 sample is as high as that over the WO_3 sample, which can be mainly attributed to the W vacancies remedy and the formation of interface WO_3/$WO_3 \cdot H_2O$ heterojunctions. This may also indicate that the defects have been remedied after being processed by H_2O_2.

Second, the H_2O_2-WO_3 sample has the largest photocurrent amongst, which can be mainly attributed to the formation of WO_3/$WO_3 \cdot 0333 H_2O$ heterojunctions (see Fig. S3, ESI). It has recently been reported that the WO_3/$WO_3 \cdot H_2O$ heterojunctions are favorable for the charge separation, thus improving the photocatalytic activity [22,35]. The *Ab* initio density functional theory (DFT) calculations have been carried out to insight the energy band structures of monoclinic WO_3 and orthorhombic $WO_3 \cdot 0.333 H_2O$. Fig. 8c and d shows their band structures calculated by the CASTEP package. The valence band maximum (VBM) and conduction band minimum (CBM) of monoclinic WO_3 are 1.8 and 0 eV, respectively; while the VBM and CBM of orthorhombic $WO_3 \cdot 0.333 H_2O$ are 2.0
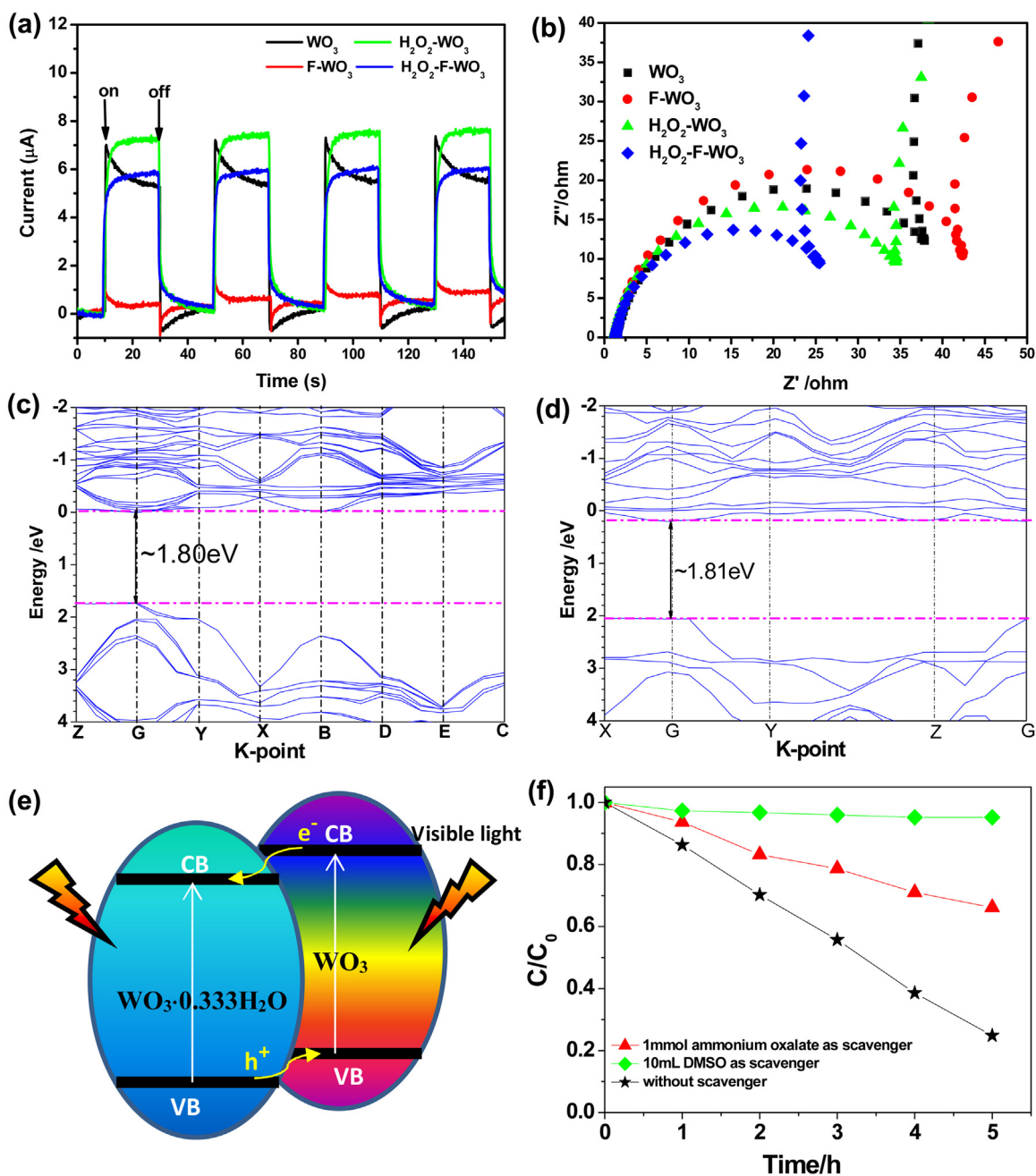
Fig. 8. (a) Photocurrent response under visible-light irradiation ($\lambda > 420$ nm) and (b) Nyquist plots of the samples; Energy band structures of (c) monoclinic WO_3 and (d) orthorhombic $WO_3 \cdot 0.333H_2O$; (e) schematic representation for the charge transfer over $WO_3/WO_3 \cdot 0.333H_2O$; and (f) trapping experiments of H_2O_2-F-WO_3.

and 0.2 eV, respectively. The direct band gaps are 1.80 and 1.81 eV for monoclinic WO_3 and orthorhombic $WO_3 \cdot 0.333H_2O$, respectively. The results confirm the monoclinic WO_3 and orthorhombic $WO_3 \cdot 0.333H_2O$ have the matched band positions. Under visible light irradiation ($\lambda > 420$ nm), the photo-generated electrons would transfer from conduction band of WO_3 to that of $WO_3 \cdot 0333H_2O$, while the holes would transfer from valence band of $WO_3 \cdot 0333H_2O$ to that of WO_3, hence, the charge separation efficiency can be efficiently improved by the $WO_3/WO_3 \cdot 0.333H_2O$ heterojunctions. The schematic representation for the charge transfer over WO3/WO3·0.333H2O is shown in Fig. 8e. However, the H_2O_2-F-WO_3 sample has a lower photocurrent than the H_2O_2-WO_3 sample, indicating that W vacancies have not been completely remedied (Table 1).

Third, it is worth mentioning that a decreasing trend can be observed for the photocurrents of the WO_3 and F-WO_3 ($R_F = 1$) samples while light-on, suggesting a quick carrier recombination on the grain surface. But the photocurrents do not decrease for the H_2O_2-WO_3 and H_2O_2-F-WO_3 samples, verifying that the $WO_3/WO_3 \cdot H_2O$ heterojunctions favor for the charge separation and transfer.

Finally, the electrochemical impedance spectra (EIS) of the samples have been measured to investigate the interface charge separation efficiency (Fig. 8b). It is well known that the separation and transfer efficiencies of photogenerated electron–hole pairs have an important influence on the photocatalytic reaction [18,36]. Amongst, the largest radius of the F-WO_3 ($R_F = 1$) sample suggests that the photogenerated electron-hole pairs are difficult to be separated and transferred [37], which may be mainly ascribed

to the formation of bulk tungsten vacancies. The arc radius of the H_2O_2-WO_3 sample is smaller than that of WO_3, verifying that the WO_3/$WO_3\cdot0.333H_2O$ heterojunction favors for the charge separation. Amongst, the H_2O_2-F-WO_3 sample shows the smallest arc radius, which could be mainly attributed to the synergistic effect of the defect remedy by H_2O_2 and the interfacial WO_3/$WO_3\cdot0.333H_2O$ heterojunctions. The EIS results well agree with photocatalytic performance of the samples, indicating the charge transfer and separation may be a main factor affecting photocatalytic performance in this work. In addition, H_2O_2-F-WO_3 sample shows a higher photocatalytic activity than H_2O_2-WO_3, which may be relative to the different precursor of the sample.

To further identify the degradation mechanism of H_2O_2-F-WO_3, the trapping experiment is performed. As shown in Fig. 8f, the photocatalytic activity of H_2O_2-F-WO_3 decreases when ammonium oxalate (as the hole scavenger) is added, whereas the degradation activity is almost completely inhibited with adding dimethyl sulfoxide (DMSO, •OH radical scavenger). The results manifest that both •OH radical and holes are the oxidation species, which is identical with WO_3 as reported in previous research [7].

The absorption spectra of RhB over H_2O_2-F-WO_3 during the degradation process are also provided in Fig. S8a. The characteristic absorption band of RhB is at about 554 nm. Two probable decomposition reactions have been reported for the photodegradation of RhB [20,38]: one is that the conjugated structure of RhB is destructed by •OH radicals and/or holes, resulting in the decrease of the absorbance but without a wavelength shift; the other process involves N-demethylation reaction, which causes a significant blue wavelength shift [20,38]. During the degradation process, the absorbance of RhB obviously decreases with irradiation time, while the characteristic adsorption band at 554 nm does not shift. This demonstrates that the former degradation process mainly occurs in our study. In addition, the cycling experiment of H_2O_2-F-WO_3 (Fig. S8b) shows that after three cycles, the H_2O_2-F-WO_3 ($R_F = 1$) sample maintains a good stability.

3.3. Defect remedy mechanism of H_2O_2 processing

In this work, we have further investigated the effects of temperatures, time and the amounts of H_2O_2 added (Figs. S5–S7, ESI). The results show that the H_2O_2 added and temperature have great influences on the phase compositions. In fact, the post-synthesis processing reaction with H_2O_2 involves the re-dissolution and re-crystallization processes. In the synthesis of orthorhombic $WO_3\cdot0.33H_2O$ with H_2O_2, Zhou et al. [21] have also reported that H_2O_2 played a key role in the formation of orthorhombic $WO_3\cdot0.33H_2O$. Since $[O_2]^{2-}$ has a strong chelating ability [21], WO_3 can dissolve in H_2O_2 solution. During the re-dissolution and re-crystallization processes, superfluous O atoms may release to the solution. Consequently, W vacancies are successfully remedied. It is obvious that the processing with H_2O_2 can not only efficiently remedy the defects caused by the fluorination, but also favor to form the WO_3/$WO_3\cdot0.333H_2O$ heterojunctions. As a result, the H_2O_2-F-WO_3 sample shows an improved photocatalytic activity for the degradation of RhB under visible light irradiation ($\lambda > 420$ nm). Compared with conventional defect remedy method (e.g., annealing) [18], this defect remedy approach with H_2O_2 is mild, controllable and energy-saving. Therefore, this post-synthesis processing method is facile, which may be extended to develop the other efficient photocatalysts.

4. Conclusions

The post-synthesis processing method with H_2O_2 can not only remedy W vacancies, but also favor for the formation of the WO_3/$WO_3\cdot0.333H_2O$ heterojunction. Under visible light irradiation ($\lambda > 420$ nm), the activity of H_2O_2-F-WO_3 sample is 4.3 times higher than that of F-WO_3. This facile post-synthesis processing method may be extended to develop the other efficient photocatalysts.

Appendix A. Supplementary data

Supplementary data associated with this article can be found, in the online version, at http://dx.doi.org/10.1016/j.apcatb.2016.09.036.

References

[1] S. Liu, J. Yu, B. Cheng, M. Jaroniec, Adv. Colloid Interface Sci. 173 (2012) 35–53.
[2] Z.F. Huang, J. Song, L. Pan, X. Zhang, L. Wang, J.J. Zou, Adv. Mater. 27 (2015) 5309–5327.
[3] C. Di Valentin, G. Pacchioni, Acc. Chem. Res. 47 (2014) 3233–3241.
[4] K.S. Joya, Y.F. Joya, K. Ocakoglu, Angew. Chem. Int. Ed. 52 (2013) 10426–10437.
[5] P.M. Rao, L. Cai, C. Liu, I.S. Cho, C.H. Lee, J.M. Weisse, P. Yang, X. Zheng, Nano Lett. 14 (2014) 1099–1105.
[6] P. Chatchai, Y. Murakami, S.-y. Kishioka, A.Y. Nosaka, Y. Nosaka, Electrochim. Acta 54 (2009) 1147–1152.
[7] K. Jungwon, L. Chul Wee, C. Wonyong, Environ. Sci. Technol. 44 (2010) 6849–6854.
[8] T. Saison, P. Gras, N. Chemin, C. Chanéac, O. Duruphty, V. Brezová, C. Colbeau-Justin, J.-P. Jolivet, J. Phys. Chem. C 117 (2013) 22656–22666.
[9] J. Sheng, X. Li, Y. Xu, ACS Catal. 4 (2014) 732–737.
[10] J.C. Yu, J. Yu, W. Ho, Z. Jiang, L. Zhang, Chem. Mater. 33 (2002) 12–13.
[11] Q. Xiang, K. Lv, J. Yu, Appl. Catal. B: Environ. 96 (2010) 557–564.
[12] W. Ho, J.C. Yu, S. Lee, Chem. Commun. (2006) 1115–1117.
[13] J. Tang, H. Quan, J. Ye, Chem. Mater. 38 (2007) 116–122.
[14] H.-Y. Jiang, J. Liu, K. Cheng, W. Sun, J. Lin, J. Phys. Chem. C 117 (2013) 20029–20036.
[15] Y. Liu, Y. Lv, Y. Zhu, D. Liu, R. Zong, Y. Zhu, Appl. Catal. B: Environ. 147 (2014) 851–857.
[16] G. Huang, Y. Zhu, J. Phys. Chem. C 111 (2007) 11952–11958.
[17] D. Li, H. Haneda, S. Hishita, N. Ohashi, N.K. Labhsetwar, J. Fluorine Chem. 126 (2005) 69–77.
[18] D. Chen, Z. Wang, T. Ren, H. Ding, W. Yao, R. Zong, Y. Zhu, J. Phys. Chem. C 118 (2014) 15300–15307.
[19] G. Xi, J. Ye, Q. Ma, N. Su, H. Bai, C. Wang, J. Am. Chem. Soc. 134 (2012) 6508–6511.
[20] R. Shi, G. Huang, J. Lin, Y. Zhu, J. Phys. Chem. C 113 (2009) 19633–19638.
[21] L. Zhou, J. Zou, J. Yu, P. Lu, J. Wei, Y. Qian, Y. Wang, C. Yu, Cryst. Growth Des. 8 (2008) 3993–3998.
[22] M. Seifollahi Bazarjani, M. Hojamberdiev, K. Morita, G. Zhu, G. Cherkashinin, C. Fasel, T. Herrmann, H. Breitzke, A. Gurlo, R. Riedel, J. Am. Chem. Soc. 135 (2013) 4467–4475.
[23] R. Abe, H. Takami, N. Murakami, B. Ohtani, J. Am. Chem. Soc. 130 (2008) 7780–7781.
[24] S. Bai, K. Zhang, L. Wang, J. Sun, R. Luo, D. Li, A. Chen, J. Mater. Chem. A 2 (2014) 7927–7934.
[25] J.F. Al-Sharab, R.K. Sadangi, V. Shukla, S.D. Tse, B.H. Kear, Cryst. Growth Des. 9 (2009) 4680–4684.
[26] D. Li, H. Haneda, N.K. Labhsetwar, S. Hishita, N. Ohashi, Chem. Phys. Lett. 401 (2005) 579–584.
[27] J. Yu, W. Wang, B. Cheng, B.L. Su, J. Phys. Chem. C 113 (2009) 6743–6750.
[28] Y. Chen, F. Chen, J. Zhang, Appl. Surf. Sci. 255 (2009) 6290–6296.
[29] Z. Zhao, X. Zhang, G. Zhang, Z. Liu, D. Qu, X. Miao, P. Feng, Z. Sun, Nano Res. 8 (2015) 4061–4071.
[30] L. Liang, K. Li, C. Xiao, S. Fan, J. Liu, W. Zhang, W. Xu, W. Tong, J. Liao, Y. Zhou, B. Ye, Y. Xie, J. Am. Chem. Soc. 137 (2015) 3102–3108.

[31] Q. Wang, C. Chen, D. Zhao, W. Ma, J. Zhao, Langmuir 24 (2008) 7338–7345.
[32] Y. Zhang, Z. Tang, X. Fu, Y. Xu, Acs Nano 4 (2010) 7303–7314.
[33] M. Kong, Y. Li, X. Chen, T. Tian, P. Fang, F. Zheng, X. Zhao, J. Am. Chem. Soc. 133 (2011) 16414–16417.
[34] X. Pan, M.Q. Yang, X. Fu, N. Zhang, Y.J. Xu, Nanoscale 5 (2013) 3601–3614.
[35] J. Cao, B. Luo, H. Lin, B. Xu, S. Chen, Appl. Catal. B: Environ. 111–112 (2012) 288–296.

[36] J. Yan, G. Wu, N. Guan, L. Li, Z. Li, X. Cao, Phys. Chem. Chem. Phys. 15 (2013) 10978–10988.
[37] L. Zhang, H. Fu, Y. Zhu, Adv. Funct. Mater. 18 (2008) 2180–2189.
[38] H. Fu, S. Zhang, T. Xu, Y. Zhu, J. Chen, Environ. Sci. Technol. 42 (2008) 2085–2091.